

# Measuring Type Ia Supernova Angular-Diameter Distances with Intensity Interferometry

A. G. Kim\* and P. E. Nugent  
*Lawrence Berkeley National Laboratory  
Berkeley, CA 94720 USA*

Xingzhuo Chen  
*Texas A&M Institute of Data Science Texas A&M University 3156 TAMU,  
College Station, TX, 77843-3156 USA*

L. Wang  
*Department of Physics and Astronomy 4242 TAMU  
College Station, TX 77843-4242 USA*

J. T. O'Brien  
*Department of Astronomy University of Illinois Urbana-Champaign  
Champaign, IL 61801-3633 and  
TARDIS Collaboration*

This paper investigates the potential of intensity interferometry, based on the Hanbury Brown-Twiss effect, for measuring supernova sizes and distances. Through optimized telescope positioning, observing strategy, and advancements in single-photon detection technology, this method can provide precise angular size measurements of Type Ia supernovae as bright as 12 mag, corresponding to a local volume out to  $z \sim 0.004$ , with an anticipated rate of  $\sim 1$  events per year. The combination of angular size data with known physical dimensions enables accurate distance determination. Multiple telescope pairs at different relative positions allow tomographic mapping of the ejecta structure while reducing distance uncertainties. As Type Ia supernovae serve as standardizable candles for measuring the Universe's expansion history, combining intensity interferometry distances with the supernova Hubble diagram facilitates measurements of the Hubble constant  $H_0$ .

## I. INTRODUCTION

Intensity interferometry, founded on the Hanbury Brown-Twiss effect [1, 2] (known as the GGLP effect in particle physics [3]), has gained renewed interest with successful measurements coming from the Cherenkov telescopes VERITAS, MAGIC, and H.E.S.S. [4–9] and deployments at 1 to 2-m class telescopes [5, 10, 11]. The success is largely due to the emergence of fast single-photon detector arrays using either single-photon avalanche detectors (SPAD) [12–14] or superconducting nanowire single-photon detectors (SNSPD) [5, 15–17]. These technologies facilitate multiplexed, precise time-correlation measurements across telescopes [18–20]. These advancements enable new scientific reach for the field of astronomical astrometry [21].

The primary observables in intensity interferometry are the correlations of photon streams at different positions. The coherence of optical waves at different coordinates and times can be decomposed into baseline (physical separation) and time-lag contributions. The time-lag contribution is what gives rise to the Hanbury Brown-Twiss effect. The light detected from astronomical sources have coherent temporal fluctuations that are directly related to the transmitted spectrum. Two telescopes observing the same source over a common time period and passband measure the same fluctuations, which gives rise to a coherence in their time-dependent signals. The baseline contribution to coherence depends on the interference pattern produced by the light emission as a function of angular position. This pattern is neither limited by atmospheric seeing nor the telescope diffraction limit, and its measurement with large telescope baselines provides angular resolutions that are difficult to obtain from a single telescope. In intensity interferometry the signal is photon counts, a local measurement that does not require the combination of light from different telescopes, which allows for multiple and distant baselines that are technically difficult to achieve in Michelson interferometry.

This study examines the telescope apertures and baselines necessary for applying intensity interferometry to measure angular diameter distances to Type Ia supernovae (SNe Ia). Such measurements will localize the 3-dimensional position

---

\* agkim@lbl.gov

of SN host galaxies. In addition, distances to Type Ia supernovae (SNe Ia), which serve as standardizable candles [22], calibrate their absolute magnitudes, providing a direct pathway to measuring  $H_0$ . We confine ourselves to the study of supernovae brighter than 12 mag, fainter than which would stress the capabilities of foreseeable next-generation observatories. Our results scope the basic requirements for a purpose-built array designed for this science case.

A reasonable number of  $< 12$  mag SNe are available for the patient astronomer. SNe Ia have a rate of  $r_v = 2.43 \times 10^{-5} \text{ SNe yr}^{-1} \text{ Mpc}^{-3} h_{70}^3$  [23] and on average reach a peak absolute magnitude of  $B = -19.13 - 5 \log(h_{70})$  [24]. These parameters set the volume and thus the numbers of supernovae available to a survey with limiting magnitude  $m_{\text{lim}}$  assuming they are standard candles: they are plotted in Figure 1. For  $m_{\text{lim}} = 12$  mag, the maximum detection depth is  $z = 0.004$  within which  $\sim 0.5$  SNe Ia are expected annually over the full sky. Since supernovae are not perfect standard candles, a differentially larger volume of intrinsically brighter but more distant objects can satisfy the detection limit. A direct estimate of the SN Ia rate based on a query to the Weizmann Interactive Supernova Data Repository [25] gives 10 normal SNe Ia with  $m \leq 12$  mag over the last 15 years, with increased frequency compared to prior years following the implementation of the PTF, iPTF, and ZTF [26–28] transient searches. Given active searches covering both hemispheres, we expect to discover  $\sim 1$  SNe Ia each year with  $m \leq 12$  mag at redshifts distributed around the curve in Figure 1. The location of the observatory dictates what fraction of these supernovae are visible.

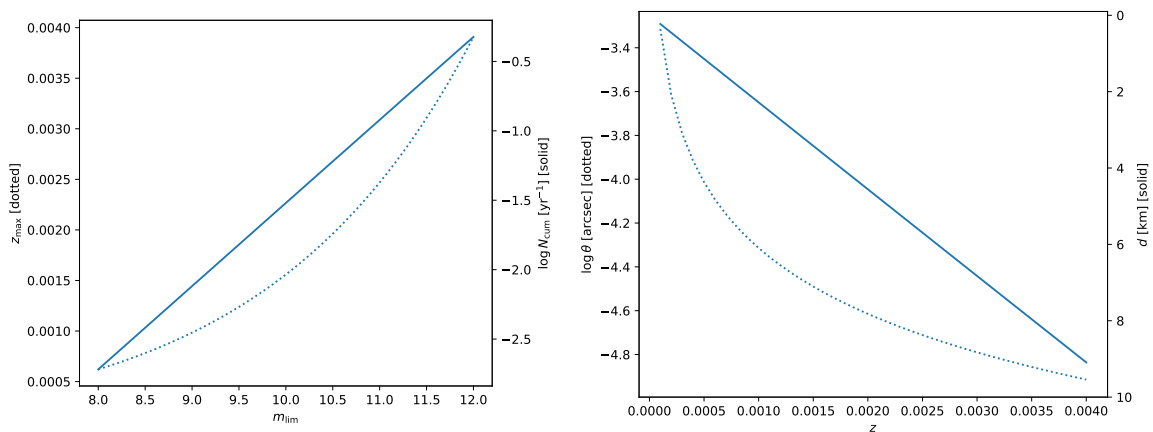


FIG. 1. Left: Cumulative full-sky rate  $N_{\text{cum}}$  (solid line) and redshift depth (dotted line) of SNe Ia as a function of survey limiting magnitude  $m_{\text{lim}}$ . Right: Angular size at maximum light (dotted line) and telescope baseline (solid line) needed to resolve SNe Ia at  $\lambda = 4400 \text{ \AA}$  as a function of redshift.

Supernovae at maximum light at these distances can be spatially resolved with telescopes separated by  $\lesssim 10$  km. The angular size of a supernova at maximum is twice the product of the photospheric velocity, say taken from the blue trough of the signature SiIII P-Cygni profile in spectra, and the time after explosion measured from the light curve. SNe Ia exhibit a photospheric velocity of  $\sim 10,000 \text{ km s}^{-1}$  [29] and reach peak brightness  $\sim 20$  days after explosion [30]. The angular resolution  $\theta$  of optical intensity interferometers is set by the diffraction limit:

$$\theta = 1.22 \frac{\lambda}{\rho}, \quad (1)$$

where  $\lambda$  represents wavelength and  $\rho$  the distance between telescopes. Angular sizes at maximum light and the required telescope baselines are plotted in Figure 1 for  $\lambda = 4400 \text{ \AA}$ . Resolving SNe Ia out to  $z = 0.004$  requires a baseline of less than 10 km. The requisite distances are higher/lower before/after peak brightness.

While core-collapse supernovae occur more frequently, their fainter intrinsic brightness confines them to a smaller volume. SNe Ia dominate magnitude-limited samples in the local universe, making them our focus.

This article explores the feasibility of measuring supernova angular sizes. §II presents light-emission profiles of an SN Ia at maximum light generated by two spectral synthesis codes. The expected intensity interferometry signal due to these two profiles are shown in §III. §IV provides the predicted precision in supernova distance for a fiducial telescope-instrument combination and discusses bias due to model inaccuracy and polarization. Conclusions are given in § V.

## II. MODELING THE SUPERNOVA EMISSION PROFILE

Intensity interferometry does not convey the phase information otherwise available when interfering electromagnetic fields, and interpretation of the measurements depends on understanding the source’s emission profile. Supernovae, as exploding stars, emit light through various physical processes occurring in an expanding medium. Their emission profile is wavelength-dependent and varies across different lines-of-sight toward the supernova surface, as atomic line transitions undergo Doppler shifts based on the velocity component directed toward the observer. As such, supernovae neither have a sharp edge nor have a constant emission over its surface. When it comes to supernovae we do not think of size, but rather a wavelength-dependent, non-uniform emission profile whose angular extent is to be measured.

In this section we present the normalized emission profiles generated by two spectral synthesis packages. Both qualitatively reproduce observed spectra, particularly the positions and shapes of the P-Cygni profiles of several atomic species. As such, they offer an improvement over measuring supernova size directly from the data. Ongoing efforts seek to refine these codes’ initial conditions and underlying physics, with the ultimate goal of achieving quantitative consistency between different models and observational data. We consider both approaches here, as they illuminate complementary aspects of the analysis. Alternatively, simpler models that focus on wavelengths corresponding to optically thick lines may suffice for our application.

The emission profiles provided by the models are denoted as  $I_M(r_1, r_2)$ , where  $r = \sqrt{r_1^2 + r_2^2}$  is the impact parameter in distance units and the components 1 and 2 are for an arbitrary polar basis. The profile of the supernova at distance  $d$  in angular position on the sky is  $I(\theta_1, \theta_2) \propto I_M(\theta_1 d, \theta_2 d)$ .

### A. TARDIS

A notable example in Type Ia supernova modeling is the analysis of SN2011fe using TARDIS, a modular, open-source, steady-state, Monte Carlo radiative-transfer spectral synthesis code for models of supernova ejecta [31]. TARDIS’ strength is speed, which allows the fitting of supernova parameters to generate an individualized model from data of a single supernova. Speed comes at the expense of making several simplifying assumptions that do not fully apply to supernovae, including spherical symmetry, no time dependence, and a photosphere that sources the energy packets. Despite these limitations, TARDIS has been used to generate models that are consistent with spectroscopic observations in the wavelength and phase regime relevant here.<sup>1</sup> Recent applications demonstrate TARDIS’s capabilities [32, 33]. Neural-network based modeling of supernova spectra has revealed correlations between radioactive <sup>56</sup>Ni and light curve properties of SNe and has derived the chemical abundances in the ejecta above the photosphere.

The example SN2011fe model’s ejecta composition and density profile are the maximum likelihood sample from generative tomographic inference by O’Brien *et al.* 2024 (in prep). The ejecta density and nuclear decay products are evolved to the peak B-band time since explosion from Pereira *et al.* [34] with the corresponding input bolometric luminosity. The inner photospheric velocity boundary is set such that the Rosseland mean optical depth is  $\frac{2}{3}$  through the ejecta above. TARDIS is run on the SN2011fe model with atomic data from Kurucz GFALL [35] and line interactions are handled by the `macroatom` model [36]. Plasma ionization populations are solved through the `nebular` approximation [37] and approximate NLTE excitation populations are solved with the `dilute-lte` prescription [38]<sup>2</sup>. Line-intensity maps as a function of impact parameter are computed from the converged mean intensity in each line’s extreme blue wing and the source function from the converged level-populations and Einstein coefficients of the TARDIS simulation following the steps for the formal integral computation [38] but without performing the final integration step. Lines of sight are drawn through a spherically-symmetric ejecta at each frequency and impact parameter, accumulating intensity with the optical depth within each shell, until exiting the ejecta. A more thorough description of the procedure can be found in the TARDIS documentation [39].

Figure 2 displays the emission at maximum light for the SN2011fe model, showing emission as a function of impact parameter  $r$  (recall TARDIS assumes spherical symmetry). In the same figure, selected wavelength slices illustrate the varying radial profiles characteristic of the expanding supernova atmosphere. Figure 3 presents the emission spectrum integrated over the full supernova surface, which can be compared with observations by the Nearby Supernova Factory 2.7 days after maximum [34]. There is excess flux calculated by TARDIS redward of 6500Å, which will be later shown to give excess intensity interferometry signal.

<sup>1</sup> A list of TARDIS-based publications is compiled at [https://tardis-sn.github.io/tardis/resources/research\\_done\\_using\\_TARDIS/research\\_papers.html](https://tardis-sn.github.io/tardis/resources/research_done_using_TARDIS/research_papers.html)

<sup>2</sup> See documentation for TARDIS at <https://tardis-sn.github.io/tardis/> for complete descriptions of configuration options

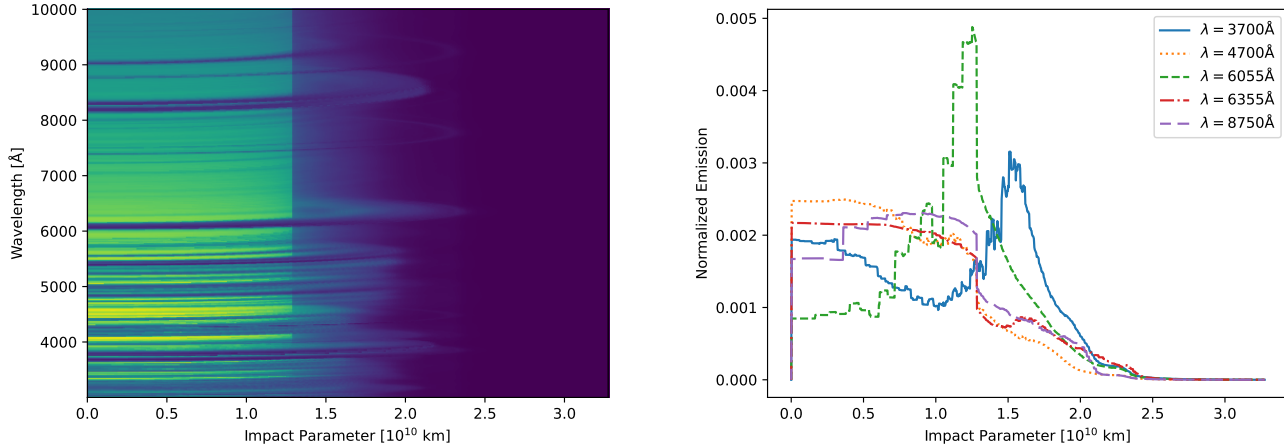


FIG. 2. Left: Model emission of SN 2011fe at maximum light generated by TARDIS as a function of impact parameter along the line of sight. Right: Normalized emission as a function of impact parameter for the same model, with selected wavelengths demonstrating the contrast in radial profiles.

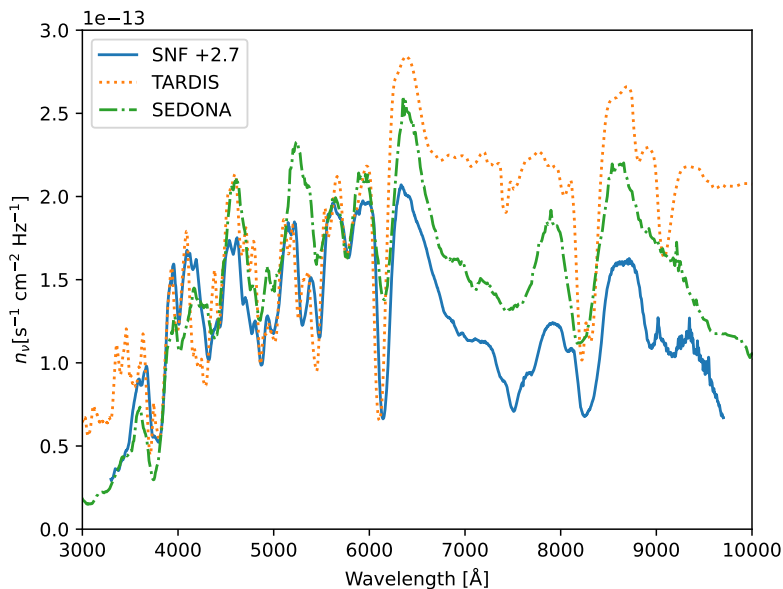


FIG. 3. Type Ia supernova photon flux density per frequency at maximum light calculated by TARDIS and SEDONA models, normalized to B-band magnitude  $B = 12.0$ . The observed spectrum from the Nearby Supernova Factory taken 2.7 days after maximum light is plotted for reference.

## B. SEDONA

The SEDONA code solves the 3-dimensional time-dependent radiative transfer problem in rapidly expanding supernova atmospheres including  $\gamma$ -ray deposition from radioactive materials to calculate lightcurves, spectra, and polarization of aspherical supernova models [40]. As such, SEDONA provides a more precise model of supernovae than TARDIS, though at greater computational expense. A comprehensive comparison between TARDIS and SEDONA can be found in Blondin *et al.* [41].

We use an upgraded version of SEDONA to simulate the N100 model, where asymmetry seeded by randomly placed ignition sites [42]. The spectropolarimetry signal retrieval method is integral-based algorithm (IBT) [43]. The

plasma excitation and ionization state is calculated using a spectral line data base with 35,344,426 spectral lines and 497,424 levels in total. The level population of Si, S, and Ca are calculated with non-local thermodynamic equilibrium (NLTE), other elements are calculated assuming local thermodynamic equilibrium (LTE) approximation. To accelerate the NLTE calculation in the 3-D simulation, we utilize a deep-learning-based algorithm. A convolutional neural network (CNN), which predicts the absorption and emission coefficient using angle-averaged specific intensity ( $J_\nu$ ) and elemental abundances as input, is trained and validated on the SEDONA radiative-transfer results of 119 1-D SNe Ia models. CNN has reduced the NLTE computation time from 72 core-seconds to 0.17 core-seconds per zone, allowing us to perform a 3-D time-dependent NLTE radiative transfer simulation. Details will be reported in Chen (in prep.).

SEDONA generates time-dependent and wavelength-dependent emission profiles. Figure 4 displays profiles at maximum light for selected wavelengths chosen to illustrate diverse emission behaviors. These wavelengths differ from those used in the TARDIS simulation to highlight SEDONA-specific features. Like the TARDIS simulation, the profiles show clear radial dependence. However, SEDONA reveals an additional characteristic: the intensities lack axial symmetry. Figure 3 presents the spectrum at maximum light integrated over the complete supernova surface.

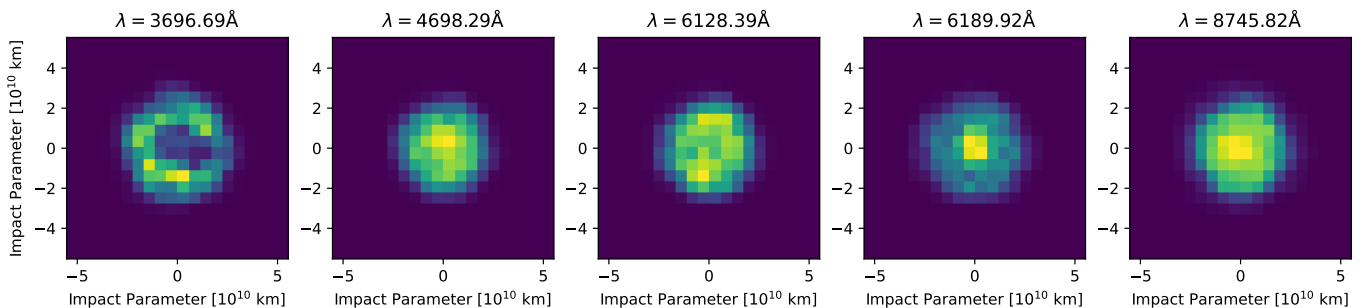


FIG. 4. SEDONA emission profiles at selected wavelengths 20 days after explosion (corresponding to the peak of the broadband light curve), showing the contrast in profile shapes.

### III. NORMALIZED VISIBILITY

The supernova's profile in angular position on the sky is denoted as  $I(\lambda, \theta_1, \theta_2)$ . The intensity interferometry signal is proportional to  $\mathcal{V}^2$ , where the normalized visibility is defined as the Fourier transform

$$\mathcal{V}(\lambda, u, v) \stackrel{\mathcal{F}}{\Leftrightarrow} \frac{I(\lambda, \theta_1, \theta_2)}{\int I(\lambda, \theta_1, \theta_2) d\theta_1 d\theta_2}, \quad (2)$$

where the Fourier transform variables  $u-v$  span a coordinate system that gives the relative telescope positions on a plane perpendicular to the line of sight. For example, a light profile  $I$  that is a uniform circle with angular diameter  $\theta$  yields the Airy profile

$$\mathcal{V}^2(u, v) = \left( \frac{2J_1(\zeta)}{\zeta} \right)^2, \quad (3)$$

where  $\zeta = \pi\rho\theta/\lambda$  and  $\rho = \sqrt{u^2 + v^2}$ ; this relationship gives rise to the resolution condition  $\theta = 1.22\lambda/\rho$ .

As shown in §II, supernova expansion creates a non-uniform emission profile, resulting in  $\mathcal{V}^2$  that varies with wavelength and deviates from an Airy disk. In the TARDIS model, the axially symmetric emission profile produces a corresponding symmetric visibility that depends on telescope separation. Figure 5 presents  $\mathcal{V}^2$  for select wavelengths. While the expected signal differs from an Airy disk—demonstrating the value of spectral synthesis codes for improved precision—it resembles one sufficiently to justify applying the resolution criterion from Eq. 1 to supernovae.

For the SEDONA emission maps,  $\mathcal{V}^2$  calculations reveal wavelength-dependent patterns. Figure 6 displays  $\mathcal{V}^2$  for select wavelengths, while Figure 7 shows  $\mathcal{V}^2$  slices at  $v = 0$ . As with TARDIS, these profiles exhibit wavelength-dependent deviations from an Airy profile. The asymmetric profile manifests in differences at the level of  $\lesssim 0.05$ .

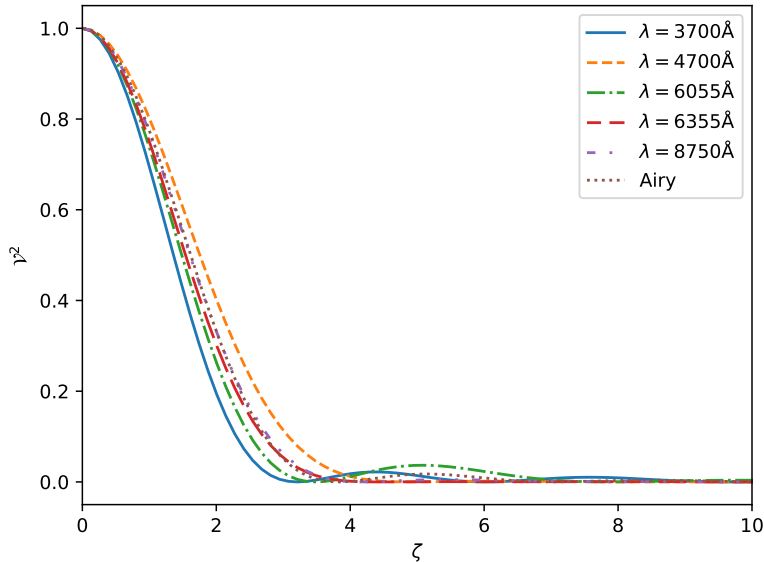


FIG. 5.  $\mathcal{V}^2$  for the TARDIS emission profile as a function of telescope separation at various wavelengths, where  $\zeta = \pi\rho\theta/\lambda$  and  $\theta$  corresponds to  $2\times$  the impact parameter of  $0.875 \times 10^{10}$  km. The Airy disk profile is shown for reference.

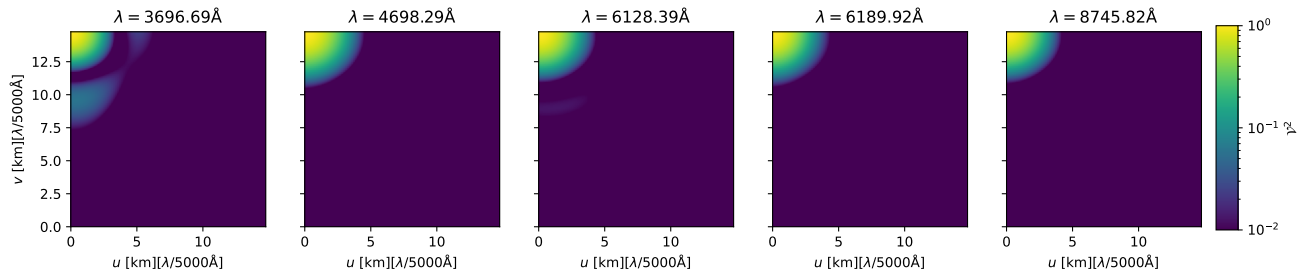


FIG. 6. Maps of the intensity interference signal  $\mathcal{V}^2$  as function of relative telescope position  $u-v$  at selected wavelengths for the SEDONA model. Values of  $u$  and  $v$  are scaled for a supernova at  $z = 0.004$ .

#### IV. DISTANCE PRECISION

In intensity interferometry a single telescope measures a series of photon counts  $N$  in a narrow frequency bin. The key measurement statistic is the covariance between the time-dependent counts from two telescopes  $\langle \delta N_1 \delta N_2 \rangle$ . For an unpolarized source with specific flux  $F_\nu$  at central frequency  $\nu_0$  and bandwidth  $\Delta\nu$ , and given a total observing time  $T_{\text{obs}}$ , Dalal et al. [44] present the signal-to-noise as:

$$\text{SNR} = \frac{\mathcal{V}^2}{\sigma_{\mathcal{V}^2}}, \quad (4)$$

where in the Poisson-noise limit and  $\sigma_I \gg \Delta\nu$

$$\sigma_{\mathcal{V}^2}^{-1} = \frac{d\Gamma}{d\nu} \left( \frac{T_{\text{obs}}}{\sigma_t} \right)^{1/2} (128\pi)^{-1/4}. \quad (5)$$

Here  $d\Gamma/d\nu = \epsilon A F_\nu / (h\nu_0) = \epsilon A n_\nu$  (proportional to the spectra plotted in Figure 3),  $\epsilon$  is the total system throughput, and  $A$  is the effective telescope area. To simplify notation, we consider the “signal” to be  $\mathcal{V}^2$  rather than  $\langle \delta N_1 \delta N_2 \rangle$ .

The noise has the feature of being independent of bandwidth when dominated by timing jitter, when the detector cannot resolve the higher-frequency temporal coherence associated with broader bandpasses. For a detector jitter of

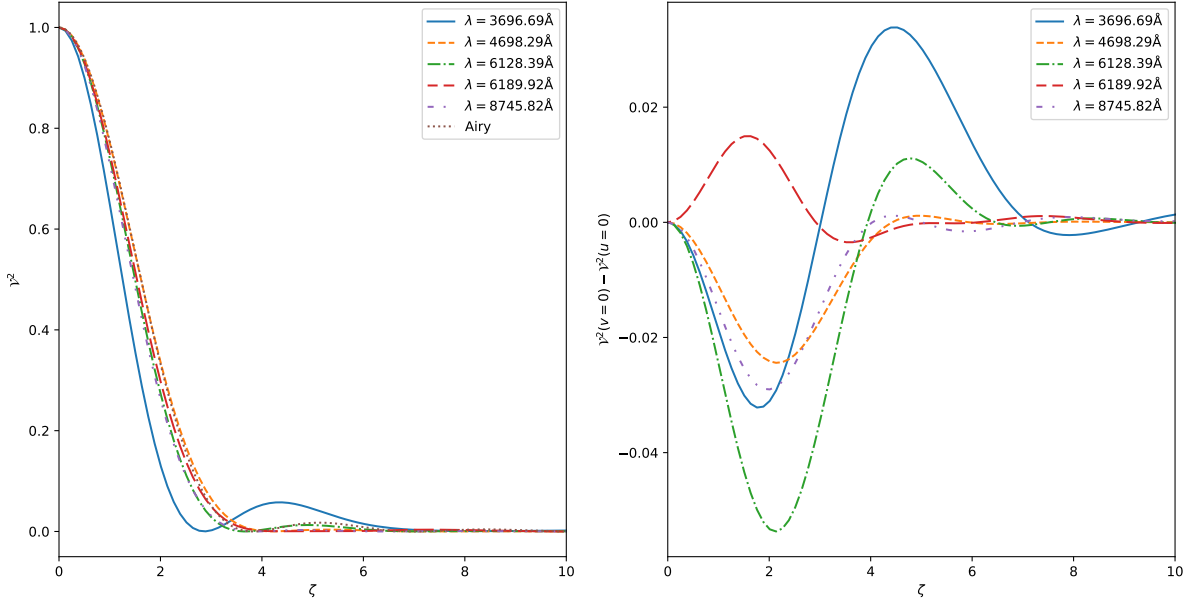


FIG. 7.  $\mathcal{V}^2$  for the SEDONA profiles at selected wavelengths. Left: Slices for  $v = 0$  with the Airy profile is shown for reference. Right: Difference between two slices  $\mathcal{V}^2(v = 0) - \mathcal{V}^2(u = 0)$ .

30 ps FWHM, this condition is  $R \ll 7000$  at optical wavelengths. We can thus consider light filtered at a resolution ( $R > 100$ ) that does not appreciably smear the interference pattern of the central frequency. Note that this feature allows us to disperse the light without noise degradation, enabling multiplex advantage through simultaneous timing measurements at different wavelengths with a detector array.

The emission profile projected onto the sky is given by  $I(\theta_1, \theta_2) \propto I_M(\theta_1 d, \theta_2 d)$ , where  $d$  represents the supernova distance. For computational convenience, we parameterize the distance as  $d = s d_0$  and where  $d_0$  is a fiducial distance and identify  $I_0(\theta_1, \theta_2) \propto I_M(\theta_1 d_0, \theta_2 d_0)$  and its corresponding visibility  $\mathcal{V}_{I_0}$ . The model for the emission profile can then be expressed as  $I(\theta; s) \propto I_0(s\theta)$  with its Fourier transform's square representing the model signal.

With the model signal and measurement uncertainty established, we can calculate the uncertainty in relative distance  $s$  to the supernova using the Fisher matrix formalism. We analyze the TARDIS and SEDONA profiles separately to highlight the distinctions between axially symmetric and asymmetric profiles.

### A. TARDIS

The intensity profile for the supernova at distance  $d = s d_0$  is given by  $I(\theta; s) \propto I_0(s\theta)$ . The normalized visibility is

$$\mathcal{V}_I(\rho; s) = \mathcal{V}_{I_0}\left(\frac{\rho}{s}\right), \quad (6)$$

where  $\rho = \sqrt{u^2 + v^2}$  and axial symmetry is assumed.

The derivative of the expected signal  $\mathcal{V}_I^2$  with respect to  $s$  can be expressed in terms of the fiducial profile as follows

$$\frac{d\mathcal{V}_{I_0}}{d\rho}(\rho) = -(2\pi)^2 \int_0^\infty I_0(\theta) J_1(2\pi\rho\theta) \theta^2 d\theta \quad (7)$$

$$\frac{d\mathcal{V}_I}{ds}(\rho) = -\frac{1}{s} \rho' \frac{d\mathcal{V}_{I_0}}{d\rho'}(\rho') \quad (8)$$

$$\frac{d\mathcal{V}_I^2}{ds}(\rho) = 2\mathcal{V}_I^* \frac{d\mathcal{V}_I}{ds}(\rho), \quad (9)$$

where  $\rho' = \rho/s$ . Using the above, the Fisher estimate for the SNR of  $s$  is

$$\text{SNR}_s = \sigma_{\mathcal{V}^2}^{-1} \left| 2\mathcal{V}_I^* \frac{d\mathcal{V}_I}{ds} \right|. \quad (10)$$

For the case of a circular aperture where the signal for a telescope pair is an Airy disk of Eq. 3,

$$\mathcal{V} = \frac{2J_1(\zeta)}{\zeta} \quad (11)$$

$$\frac{d\mathcal{V}_s}{ds} = -\frac{1}{s} \zeta' \left( \frac{J_0(\zeta')}{\zeta'} - \frac{J_2(\zeta')}{\zeta'} - \frac{2J_1(\zeta')}{\zeta'^2} \right) \quad (12)$$

so

$$\text{SNR}_s = 2\sigma_{\mathcal{V}^2}^{-1} \left| \frac{2J_1(\zeta')}{\zeta'} \left( J_0(\zeta') - J_2(\zeta') - \frac{2J_1(\zeta')}{\zeta'} \right) \right|, \quad (13)$$

where  $\zeta' = \zeta/s$ . The shape of this function is plotted in Figure 8.

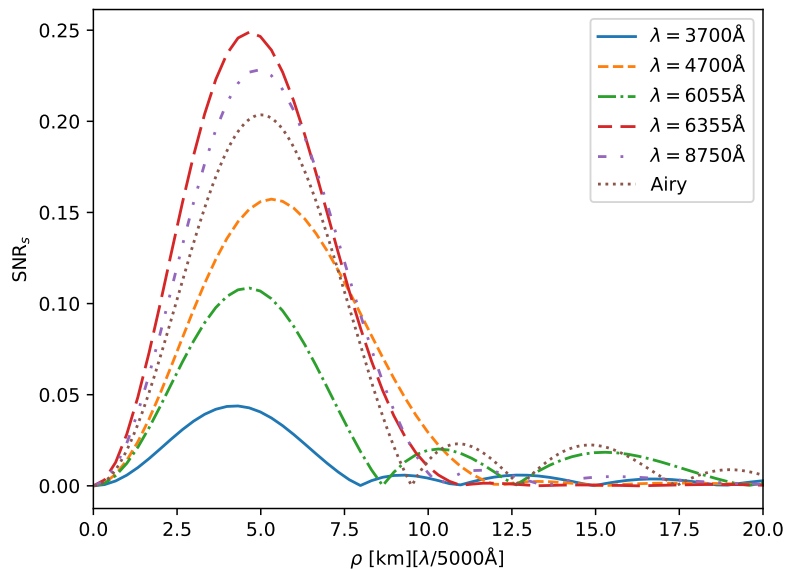


FIG. 8. Signal-to-noise of distance parameter  $s$  as a function of telescope separation  $\rho$  at selected wavelengths for the TARDIS model. The supernova is at  $z = 0.004$  with  $B = 12$  mag. Measurements assume a supernova at  $z = 0.004$  with  $B = 12$  mag, using two Keck-like telescopes with effective throughput  $\epsilon = 0.39$  and a 1-hour exposure time. The signal-to-noise function for a circular profile with radius  $0.875 \times 10^{10}$  km is shown for reference.

We adopt two Keck-like telescopes separated by a baseline distance  $\rho$  as a reference for our signal-to-noise calculations. Keck has an effective aperture of a 9.96 m diameter telescope with mirror smoothness at a level of a few nm. We assign a combined mirror reflectivity of 0.73, filter transmission of 0.9, and a detector quantum efficiency of 0.6 to give an effective total throughput of  $\epsilon = 0.39$ . Each telescope is equipped with photon counters with a timing jitter of 30 ps FWHM or  $\sigma_t = 13$  ps RMS. For the moment only a single wavelength channel is considered, although spectral multiplexing is possible.

Our reference Keck-like telescope pair can be translated to a larger number of small-aperture telescopes. The signal-to-noise from single baseline is proportional to the collecting area. The combined signal-to-noise of  $B$  baselines is proportional to  $\sqrt{B}$ , where the number of baselines is  $B = \binom{N}{2}$  and  $N$  is the number of telescopes. With these scalings, the signal-to-noise of two 10m telescopes is achieved with 566 0.5m, 142 1m, or 36 2m telescopes. Alternatively, distributing the primary mirror area from two large aperture telescopes to increasing numbers of smaller telescopes improves the signal-to-noise by up to a factor  $\sqrt{2}$ .

The source is modeled as a supernova at  $z = 0.004$  with  $B = 12$  mag and an emission profile given by TARDIS. These parameters, together with the exposure time, determine the noise  $\sigma_{\mathcal{V}^2}$ . The signal to noise of the  $s$  parameter as

a function of telescope separation is computed for a one hour observation  $T_{\text{obs}} = 1$  h exposure is shown in Fig. 8. The distance is best constrained with telescope separations where the gradient in the signal is steepest and at wavelengths where  $n_\nu$  is highest, with the caveat that TARDIS overestimates flux for wavelengths redward of 6500 Å as shown in Figure 3. The signal to noise can be increased with multiple exposures and wavelength multiplexing. For signal-to-noise of order 0.15 per measurement, a factor of  $133^2$  independent measurements are needed to achieve a total  $\text{SNR} \approx 20$  enabling a 5% precision on the distance, comparable to the intrinsic dispersion from SNe Ia.

## B. SEDONA

In this section we consider the SEDONA calculated emission profile, which lacks axial symmetry. We will show that the statistical size constraints approach those of the 1-dimensional model considered in the previous section. The more important point of focus are the features that arise when the supernova emission is not symmetric.

The model intensity profile requires an extra parameter  $\phi$  to specify its orientation in the sky. We again consider distances relative to an initial estimate  $d_0$ , so that distance parameter is  $s = d/d_0$ . The intensity profile for the supernova is expressed as  $I(\theta_1, \theta_2; s, \phi) \propto I_0(s(\theta_1 \cos \phi - \theta_2 \sin \phi), s(\theta_1 \sin \phi + \theta_2 \cos \phi))$  and

$$\mathcal{V}_I(u, v; s) = \mathcal{V}_{I_0} \left( \frac{u \cos \phi - v \sin \phi}{s}, \frac{u \sin \phi + v \cos \phi}{s} \right). \quad (14)$$

The partial derivatives of  $\mathcal{V}_I$  with respect to  $s$  and  $\phi$  can be expressed in terms of the fiducial profile as follows

$$\frac{\partial \mathcal{V}_{I_0}}{\partial u}(u, v) = -i2\pi \int \int \theta_1 I_0(\theta_1, \theta_2) e^{-i2\pi(u\theta_1 + v\theta_2)} d\theta_1 d\theta_2 \quad (15)$$

$$\frac{\partial \mathcal{V}_I}{\partial s}(u, v) = -\frac{1}{s} \left( u' \frac{\partial \mathcal{V}_{I_0}}{\partial u'}(u', v') + v' \frac{\partial \mathcal{V}_{I_0}}{\partial v'}(u', v') \right) \quad (16)$$

$$\frac{\partial \mathcal{V}_I}{\partial \phi}(u, v) = -v' \frac{\partial \mathcal{V}_{I_0}}{\partial u'}(u', v') + u' \frac{\partial \mathcal{V}_{I_0}}{\partial v'}(u', v'), \quad (17)$$

where  $u' = (u \cos \phi - v \sin \phi)/s$  and  $v' = (u \sin \phi + v \cos \phi)/s$ . The Fisher matrix is

$$F = \sigma_{\mathcal{V}^2}^{-1} \begin{pmatrix} \sum \left( \frac{\partial \mathcal{V}_I^2}{\partial s} \right)^2 & \sum \frac{\partial \mathcal{V}_I^2}{\partial s} \frac{\partial \mathcal{V}_I^2}{\partial \phi} \\ \sum \frac{\partial \mathcal{V}_I^2}{\partial s} \frac{\partial \mathcal{V}_I^2}{\partial \phi} & \sum \left( \frac{\partial \mathcal{V}_I^2}{\partial \phi} \right)^2 \end{pmatrix}, \quad (18)$$

where the summation is over independent measurements. The estimate for the SNR of  $s$  is

$$\text{SNR}_s = (F_{ss}^{-1})^{-1/2}. \quad (19)$$

At least two pairs of measurements are necessary to measure the two parameters of the model. Two observing strategies are considered. In the first strategy there are two baselines perpendicular to each other. Each baseline has a thirty minute exposure, resulting in a total exposure time of one hour for both pairs. The second strategy uses three baselines obtained from three telescopes positioned at the vertices of a right isosceles triangle. Two pairs have the same separation and orientations  $90^\circ$  relative to each other, while the third pair has a  $45^\circ$  orientation and a  $\sqrt{2}$  separation relative to the others. In this case, each pair has a twenty minute exposure again giving a total exposure time of one hour. Both strategies use the same telescopes and detectors described in §IV A.

The resulting signal-to-noise maps for selected wavelengths are presented in Figure 9. The  $u$ - $v$  coordinate corresponds to one of the pairs with equal separation. White points in the maps indicate locations where the Fisher matrix inversion encounters numerical exceptions, which occurs when derivatives with respect to  $\phi$  are small. (An axially symmetric profile such as from TARDIS would lead to singular Fisher matrices.)

Uncertainty in the emission is explored by randomly perturbing the emission of each spatial element by  $1 \pm 0.05$ , which propagates into a signal bias  $\Delta \mathcal{V}^2$ . The same perturbation realization is applied to all wavelengths. The relative distance bias  $\delta_s$  caused by  $\Delta \mathcal{V}^2$  is given by the Fisher formalism [45] as:

$$\delta_s = F_{ss}^{-1} \sum_k \frac{\partial \mathcal{V}_k^2}{\partial s} \sigma_{\mathcal{V}^2}^{-2} \Delta \mathcal{V}_k^2 + F_{s\phi}^{-1} \sum_k \frac{\partial \mathcal{V}_k^2}{\partial \phi} \sigma_{\mathcal{V}^2}^{-2} \Delta \mathcal{V}_k^2. \quad (20)$$

The biases for both configurations are calculated and shown in Figure 9. The largest biases occur in regions with low signal-to-noise ratios.

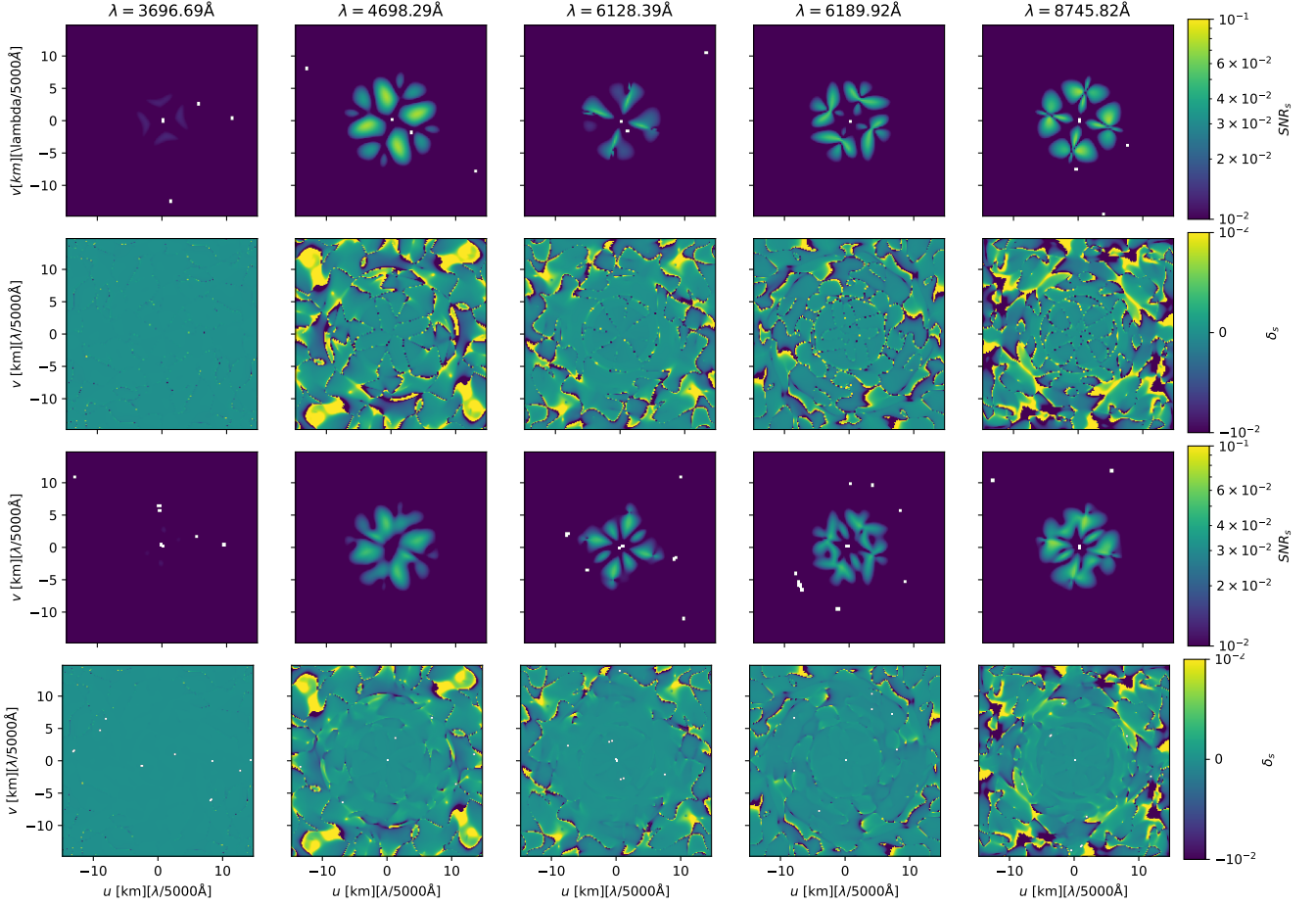


FIG. 9. Results for distance parameter  $s$  measurements using SEDONA model with the two-pair configuration (top two panels) and the three-pair configuration (bottom two panels) at selected wavelengths. Assumes a supernova at  $z = 0.004$  with  $B = 12$  mag. First and third panels: Signal-to-noise ratio of distance parameter  $\text{SNR}_s$ . Second and fourth panels: Biases in relative distance  $\delta_s$ . The  $u$ - $v$  coordinate corresponds to one of the pairs with equal separation.

The axial asymmetry of the supernova profile results in measurement precisions and biases that depend non-trivially on telescope pair orientations. The signal-to-noise map for the three-pair configuration is more evenly distributed (blurred) compared to the two-pair configuration. Additionally, the bias map for the three-pair configuration is less speckled and has lower amplitude. Increasing the number of correlation pairs with independent orientations helps mitigate systematic effects caused by profile asymmetry.

The fluctuations that give rise to the cross-correlation signal arise from fluctuations in the number of photons in each state that make up the incident wave. The derivation of Eq. 4 assumes unpolarized light, where the two polarization states with the same frequency have equal intensity. For partially polarized light, the count correlation of each polarization state must be calculated separately, and then combined to give the total signal.

The integrated polarization of SNe Ia is observed to be  $P \lesssim 0.005$ , except at wavelengths corresponding to high-velocity Ca II, where it can be higher [46]. SEDONA calculates similar integrated polarization, though with a non-trivial spatial structure. Polarization maps generated by SEDONA (Figure 10) show weak polarization toward the core, where the supernova is brightest, and strong polarization at the outer fringes, where emission is weakest. The difference between the intensity interferometry signals calculated with and without considering polarization,  $\mathcal{V}^2 - \mathcal{V}_{\text{polar}}^2$ , is also shown in Figure 10. Extreme differences are localized in  $u$ - $v$  space and are  $< 5 \times 10^{-4}$ . The relative distance bias  $\delta_s$  for both two- and three-pair configurations is  $\lesssim 0.005$  in regions with high signal-to-noise.

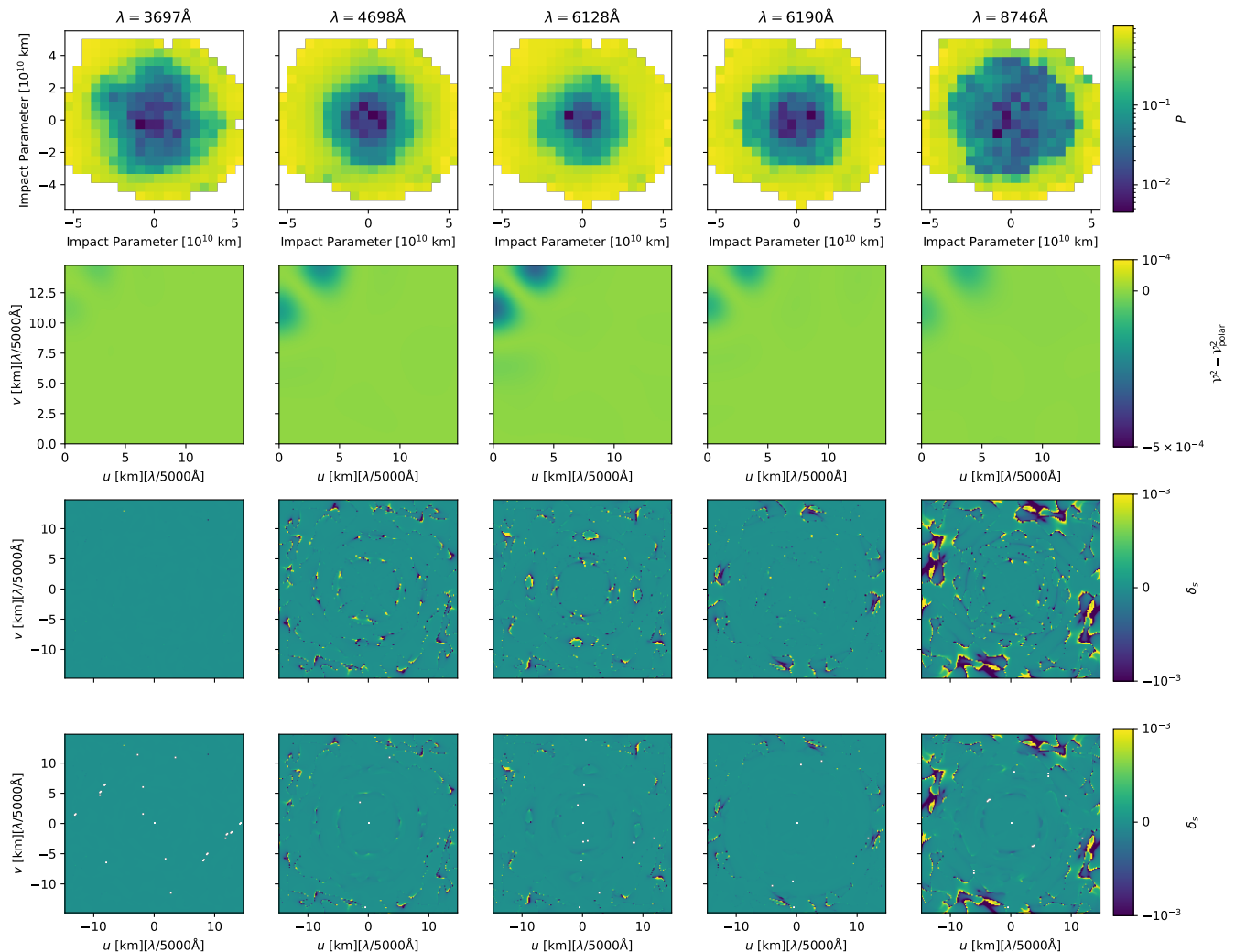


FIG. 10. Top panel: SEDONA polarization maps 20 days after explosion (at broadband light curve peak) at selected wavelengths. Second panel: Difference between expected signals with and without accounting for polarization,  $\mathcal{V}^2 - \mathcal{V}_{\text{polar}}^2$ . Second panel: Difference between expected signals with and without accounting for polarization,  $\delta_s$ , for the two-pair and three-pair configurations respectively. The  $u$ - $v$  coordinate corresponds to one of the pairs with equal separation and scaled for a supernova at  $z = 0.004$ .

## V. CONCLUSIONS

We have demonstrated the feasibility of using intensity interferometry at optical wavelengths to achieve high-precision measurements of supernova distances, leveraging upcoming observatories and advanced detectors. This approach relies on telescope arrays with large light-gathering areas but moderate optical quality, and fast, multiplexed photon detectors. Given the expected supernova rate, multiple events can be observed within the measurement volume during the lifetime of an observing campaign.

For individual SNe Ia, distance measurements combined with multi-band light curves enable the determination of the Hubble constant,  $H_0$ . The supernova distance  $d$  (measured in Mpc) and observed magnitude  $m$  are used to calculate the absolute magnitude through the relation  $M = m + 5 \log d + 25$ . Independently, light curve and/or spectroscopic data together with the SN Ia Hubble diagram are used to determine the SN's value of  $\mathcal{M}$ , using tools like the SALT2 light-curve model and magnitude calibration [47]. The Hubble constant is then derived using the relation  $\mathcal{M} = M - 5 \log H_0$ .

Further work is needed to quantify model-specific systematic errors. Comparing TARDIS and SEDONA predictions for the same supernova across common phases and viewing angles serves as a robustness check. Identifying wavelengths that are less sensitive to modeling choices would be particularly beneficial.

Much of the current activity in intensity interferometry is motivated by the availability of current (VERITAS, MAGIC, H.E.S.S.) and future Cherenkov telescopes (CTAO). Unfortunately, these telescopes are not capable of supporting the assumptions made in this article. Their coarse  $>$ arcmin point-spread function results in contamination from the background galaxy and other projected sources. The optical timing dispersion is on the order of ns, longer than the detector jitter. Cherenkov telescopes have poor throughput at red wavelengths, where the SN signal is strongest. For these reasons, we consider a Keck-like observatory designed to have a fine point-spread function and high red-IR throughput, while noting that it is likely more cost-effective to obtain good optical quality and total collecting area with a larger number of smaller-aperture telescopes.

Supernova shape evolution can be modeled and measured through multiple observations over time. These repeated measurements yield multiple distance estimates, reducing systematic uncertainties inherent to supernova modeling. In the analysis presented in this article we assumed that the phase of the supernova at the date of observation is known, say as constrained by pre- and post-explosion photometric measurements by transient searches. However, this assumption becomes unnecessary when observations are taken on different dates. Two observations can constrain the phase directly, as this information is explicit in the SEDONA model and can be reconstructed empirically from ejecta velocities derived from single-phase TARDIS fits.

Geometric distances less sensitive to the details of the physical processes may be derived based on the angular expansion rates measured from intensity interferometry and the physical size of the photosphere that can be derived from the photospheric speed measurable from normal spectroscopy. Multi-epoch intensity interferometry is needed to avoid the need for the exact time of explosion. Distances can be calculated simply by dividing the angular expansion rates of the photosphere by the corresponding photospheric velocities. However, spectroscopic models are still needed to select wavelength regions that can be robustly modeled by today's radiative transfer codes.

Core-collapse supernovae bright enough to produce an intensity interferometry signal are also expected to occur. While most core-collapse supernova subtypes are intrinsically more asymmetric than SNe Ia, Type II-P supernovae are an exception. These events generally exhibit very low polarization during their plateau phase, and their modeling is relatively straightforward due to well-understood progenitor systems [48, 49]. As such, they are valuable for distance determination using the expanding photosphere method [50–53].

## ACKNOWLEDGMENTS

We would like to thank Jeff Hodgson, Eddie Baron, Dan Kasen, Neal Dalal, and Paul Stankus for valuable discussions. This work was supported by the U.S. Department of Energy (DOE), Office of Science, Office of High-Energy Physics, under Contract No. DE-AC02-05CH11231. The SEDONA radiative transfer calculation used FASTER at TAMU through the allocation PHY240215 from the Advanced Cyberinfrastructure Coordination Ecosystem: Services & Support (ACCESS) program, which is supported by U.S. National Science Foundation grants #2138259, #2138286, #2138307, #2137603, and #2138296.

- 
- [1] R. H. Brown and R. G. Twiss, *Philosophical Magazine* **45**, 663 (1954).
  - [2] R. Hanbury Brown, *Nature* **178**, 1046 (1956).
  - [3] G. Goldhaber, S. Goldhaber, W.-Y. Lee, and A. Pais, *Phys. Rev.* **120**, 300 (1960).
  - [4] V. A. Acciari, M. I. Bernardos, E. Colombo, J. L. Contreras, J. Cortina, A. De Angelis, C. Delgado, C. Díaz, D. Fink, M. Mariotti, S. Mangano, R. Mirzoyan, M. Polo, T. Schweizer, and M. Will, *MNRAS* **491**, 1540 (2020), arXiv:1911.06029 [astro-ph.IM].
  - [5] C. Frohmaier, C. R. Angus, M. Vincenzi, M. Sullivan, M. Smith, P. E. Nugent, S. B. Cenko, A. Gal-Yam, S. R. Kulkarni, N. M. Law, and R. M. Quimby, *Monthly Notices of the Royal Astronomical Society* **500**, 5142 (2020).
  - [6] A. Zmija, N. Vogel, F. Wöhlehen, G. Anton, A. Zink, and S. Funk, *MNRAS* **527**, 12243 (2024), arXiv:2312.08015 [astro-ph.IM].
  - [7] S. Abe, J. Abhir, V. Acciari, A. Aguasca-Cabot, I. Agudo, T. Aniello, S. Ansoldi, L. Antonelli, A. Arbet Engels, C. Arcaro, *et al.*, *Monthly Notices of the Royal Astronomical Society* **529**, 4387 (2024).
  - [8] A. Acharyya, J. P. Aufdenberg, P. Bangale, J. T. Bartkoske, P. Batista, W. Benbow, A. J. Chromey, J. D. Davis, Q. Feng, J. Foote, A. Furniss, W. Hanlon, C. E. Hinrichs, J. Holder, W. Jin, P. Kaaret, M. Kertzman, D. Kieda, T. K. Kleiner, N. Korzoun, T. Lebohec, M. A. Lisa, M. Lundy, N. Matthews, C. E. McGrath, M. J. Millard, P. Moriarty, S. Nikkhah, S. O'Brien, R. A. Ong, M. Pohl, E. Pueschel, J. Quinn, P. L. Rabinowitz, K. Ragan, E. Roache, J. G. Rose, J. L. Sackrider, I. Sadeh, L. Saha, G. H. Sembroski, R. Shang, D. Tak, M. Ticores, J. V. Tucci, D. A. Williams, S. L. Wong, and VERITAS Collaboration, *ApJ* **966**, 28 (2024), arXiv:2401.01853 [astro-ph.SR].
  - [9] N. Vogel, A. Zmija, F. Wöhlehen, G. Anton, A. Mitchell, A. Zink, and S. Funk, *Monthly No-*

- tices of the Royal Astronomical Society , stae2643 (2024), <https://academic.oup.com/mnras/advance-article-pdf/doi/10.1093/mnras/stae2643/60828614/stae2643.pdf>.
- [10] L. Zampieri, G. Naletto, A. Burtovoi, M. Fiori, and C. Barbieri, *MNRAS* **506**, 1585 (2021), arXiv:2107.05596 [astro-ph.IM].
- [11] N. Matthews, J.-P. Rivet, D. Vernet, M. Hugbart, G. Labeyrie, R. Kaiser, J. Chabé, C. Courde, O. Lai, F. Vakili, O. Garde, and W. Guerin, *AJ* **165**, 117 (2023), arXiv:2301.04878 [astro-ph.IM].
- [12] L. Gasparini, B. Bessire, M. Unternährer, A. Stefanov, D. Boiko, M. Perenzoni, and D. Stoppa, in *Quantum Sensing and Nano Electronics and Photonics XIV*, Vol. 10111, edited by M. Razeghi, International Society for Optics and Photonics (SPIE, 2017) p. 101112L.
- [13] M. Perenzoni, L. Pancheri, and D. Stoppa, *Sensors* **16**, 745 (2016).
- [14] M.-J. Lee and E. Charbon, *Japanese Journal of Applied Physics* **57**, 1002A3 (2018).
- [15] A. Divochiy, F. Marsili, D. Bitauld, A. Gaggero, R. Leoni, F. Mattioli, A. Korneev, V. Seleznev, N. Kaurova, O. Minaeva, G. Gol'tsman, K. G. Lagoudakis, M. Benkhaoul, F. Lévy, and A. Fiore, *Nature Photonics* **2**, 302 (2008).
- [16] D. Zhu, M. Colangelo, C. Chen, B. A. Korzh, F. N. C. Wong, M. D. Shaw, and K. K. Berggren, *Nano Letters* (2020).
- [17] B. Korzh, Q. Zhao, J. P. Allmaras, S. Frasca, T. M. Autry, E. A. Bersin, A. D. Beyer, R. M. Briggs, B. Bumble, M. Colangelo, G. M. Crouch, A. E. Dane, T. Gerrits, A. E. Lita, F. Marsili, G. Moody, C. Peña, E. Ramirez, J. D. Rezac, N. Sinclair, M. J. Stevens, A. E. Velasco, V. B. Verma, E. E. Wollman, S. Xie, D. Zhu, P. D. Hale, M. Spiropulu, K. L. Silverman, R. P. Mirin, S. W. Nam, A. G. Kozorezov, M. D. Shaw, and K. K. Berggren, *Nature Photonics* **14**, 250 (2020).
- [18] J. Crawford, D. Dolzhenko, M. Keach, A. Mueninghoff, R. A. Abraham, J. Martinez-Rincon, P. Stankus, S. Vintskevich, and A. Nomerotski, *Optics Express* **31**, 44246 (2023), arXiv:2301.07042 [astro-ph.IM].
- [19] J. Ferrantini, J. Crawford, S. Kulkov, J. Jirsa, A. Mueninghoff, L. Lawrence, S. Vintskevich, T. Milanese, S. Burri, E. Bernasconi, C. Bruschini, M. Marcisovsky, P. Svihra, A. Nomerotski, P. Stankus, E. Charbon, and R. A. Abraham, arXiv e-prints , arXiv:2406.13959 (2024), arXiv:2406.13959 [physics.optics].
- [20] S. Tolila, G. Labeyrie, R. Kaiser, J. P. Rivet, and W. Guerin, arXiv e-prints , arXiv:2411.08417 (2024), arXiv:2411.08417 [astro-ph.IM].
- [21] P. Stankus, A. Nomerotski, A. Slosar, and S. Vintskevich, *The Open Journal of Astrophysics* **5**, 16 (2022), arXiv:2010.09100.
- [22] M. M. Phillips, *Astrophysical Journal Letters* **413**, L105 (1993).
- [23] C. Frohmaier, M. Sullivan, P. E. Nugent, M. Smith, G. Dimitriadis, J. S. Bloom, S. B. Cenko, M. M. Kasliwal, S. R. Kulkarni, K. Maguire, E. O. Ofek, D. Poznanski, and R. M. Quimby, *MNRAS* **486**, 2308 (2019), arXiv:1903.08580 [astro-ph.HE].
- [24] D. Richardson, D. Branch, D. Casebeer, J. Millard, R. C. Thomas, and E. Baron, *AJ* **123**, 745 (2002), arXiv:astro-ph/0112051 [astro-ph].
- [25] O. Yaron and A. Gal-Yam, *PASP* **124**, 668 (2012), arXiv:1204.1891 [astro-ph.IM].
- [26] N. M. Law, S. R. Kulkarni, R. G. Dekany, E. O. Ofek, R. M. Quimby, P. E. Nugent, J. Surace, C. C. Grillmair, J. S. Bloom, M. M. Kasliwal, L. Bildsten, T. Brown, S. B. Cenko, D. Ciardi, E. Croner, S. G. Djorgovski, J. van Eyken, A. V. Filippenko, D. B. Fox, A. Gal-Yam, D. Hale, N. Hamam, G. Helou, J. Henning, D. A. Howell, J. Jacobsen, R. Laher, S. Mattingly, D. McKenna, A. Pickles, D. Poznanski, G. Rahmer, A. Rau, W. Rosing, M. Shara, R. Smith, D. Starr, M. Sullivan, V. Velur, R. Walters, and J. Zolkower, *PASP* **121**, 1395 (2009), arXiv:0906.5350 [astro-ph.IM].
- [27] S. R. Kulkarni, *The Astronomer's Telegram* **11266**, 1 (2018).
- [28] E. C. Bellm, S. R. Kulkarni, M. J. Graham, R. Dekany, and et al., *Publications of the Astronomical Society of the Pacific* **131**, 018002 (2019).
- [29] S. Benetti, E. Cappellaro, P. A. Mazzali, M. Turatto, G. Altavilla, F. Bufano, N. Elias-Rosa, R. Kotak, G. Pignata, M. Salvo, and V. Stanishev, *ApJ* **623**, 1011 (2005), arXiv:astro-ph/0411059 [astro-ph].
- [30] D. Jack, P. H. Hauschildt, and E. Baron, *A&A* **528**, A141 (2011), arXiv:1105.3330 [astro-ph.SR].
- [31] W. E. Kerzendorf and S. A. Sim, *MNRAS* **440**, 387 (2014), arXiv:1401.5469 [astro-ph.SR].
- [32] X. Chen, L. Hu, and L. Wang, *ApJS* **250**, 12 (2020), arXiv:1911.05209 [astro-ph.HE].
- [33] X. Chen, L. Wang, L. Hu, and P. J. Brown, *ApJ* **962**, 125 (2024), arXiv:2210.15892 [astro-ph.HE].
- [34] R. Pereira, R. C. Thomas, G. Aldering, P. Antilogus, C. Baltay, S. Benitez-Herrera, S. Bongard, C. Buton, A. Canto, F. Cellier-Holzem, J. Chen, M. Childress, N. Chotard, Y. Copin, H. K. Fakhouri, M. Fink, D. Fouchez, E. Gangler, J. Guy, W. Hillebrandt, E. Y. Hsiao, M. Kerschhaggl, M. Kowalski, M. Kromer, J. Nordin, P. Nugent, K. Paeck, R. Pain, E. Pécontal, S. Perlmutter, D. Rabinowitz, M. Rigault, K. Runge, C. Saunders, G. Smadja, C. Tao, S. Taubenberger, A. Tilquin, and C. Wu, *A&A* **554**, A27 (2013), arXiv:1302.1292 [astro-ph.CO].
- [35] R. Kurucz and B. Bell, *Atomic Line Data* (R.L. Kurucz and B. Bell) Kurucz CD-ROM No. 23. Cambridge **23** (1995).
- [36] L. B. Lucy, *A&A* **384**, 725 (2002), arXiv:astro-ph/0107377 [astro-ph].
- [37] P. A. Mazzali and L. B. Lucy, *A&A* **279**, 447 (1993).
- [38] L. B. Lucy, *A&A* **345**, 211 (1999).
- [39] TARDIS Collaboration, *Spectrum Generation with the Formal Integral*, TARDIS Core Package Documentation (2025), [https://tardis-sn.github.io/tardis/physics/spectrum/formal\\_integral.html#calculating-i-nu-p](https://tardis-sn.github.io/tardis/physics/spectrum/formal_integral.html#calculating-i-nu-p) [Accessed: Jan 17,2025].
- [40] D. Kasen, R. C. Thomas, and P. Nugent, *ApJ* **651**, 366 (2006), arXiv:astro-ph/0606111 [astro-ph].
- [41] S. Blondin, S. Blinnikov, F. P. Callan, C. E. Collins, L. Dessart, W. Even, A. Flörs, A. G. Fullard, D. J. Hillier, A. Jerkstrand, D. Kasen, B. Katz, W. Kerzendorf, A. Kozyreva, J. O'Brien, E. A. Pássaro, N. Roth, K. J. Shen, L. Shingles, S. A. Sim, J. Singhal, I. G. Smith, E. Sorokina, V. P. Utrobin, C. Vogl, M. Williamson, R. Wollaeger, S. E. Woosley, and N. Wygoda, *A&A* **668**, A163 (2022), arXiv:2209.11671 [astro-ph.SR].
- [42] F. K. Röpkke, M. Kromer, I. R. Seitenzahl, R. Pakmor, S. A. Sim, S. Taubenberger, F. Ciaraldi-Schoolmann, W. Hillebrandt,

- G. Aldering, P. Antilogus, C. Baltay, S. Benitez-Herrera, S. Bongard, C. Buton, A. Canto, F. Cellier-Holzem, M. Childress, N. Chotard, Y. Copin, H. K. Fakhouri, M. Fink, D. Fouchez, E. Gangler, J. Guy, S. Hachinger, E. Y. Hsiao, J. Chen, M. Kerschhaggl, M. Kowalski, P. Nugent, K. Paech, R. Pain, E. Pecontal, R. Pereira, S. Perlmutter, D. Rabinowitz, M. Rigault, K. Runge, C. Saunders, G. Smadja, N. Suzuki, C. Tao, R. C. Thomas, A. Tilquin, and C. Wu, *ApJ* **750**, L19 (2012), arXiv:1203.4839 [astro-ph.SR].
- [43] X. Chen, L. Wang, and D. Kasen, arXiv e-prints , arXiv:2409.07729 (2024), arXiv:2409.07729 [astro-ph.HE].
- [44] N. Dalal, M. Galanis, C. Gammie, S. E. Gralla, and N. Murray, *Phys. Rev. D* **109**, 123029 (2024), arXiv:2403.15903 [astro-ph.CO].
- [45] E. V. Linder, *Astroparticle Physics* **26**, 102 (2006), arXiv:astro-ph/0604280 [astro-ph].
- [46] L. Wang and J. C. Wheeler, *ARA&A* **46**, 433 (2008), arXiv:0811.1054 [astro-ph].
- [47] J. Guy, P. Astier, S. Baumont, D. Hardin, R. Pain, N. Regnault, S. Basa, R. G. Carlberg, A. Conley, S. Fabbro, D. Fouchez, I. M. Hook, D. A. Howell, K. Perrett, C. J. Pritchett, J. Rich, M. Sullivan, P. Antilogus, E. Aubourg, G. Bazin, J. Bronder, M. Filiol, N. Palanque-Delabrouille, P. Ripoche, and V. Ruhlmann-Kleider, *A&A* **466**, 11 (2007), arXiv:astro-ph/0701828 [astro-ph].
- [48] T. Nagao, K. Maeda, and M. Tanaka, *ApJ* **861**, 1 (2018), arXiv:1805.11865 [astro-ph.HE].
- [49] S. J. Smartt, J. J. Eldridge, R. M. Crockett, and J. R. Maund, *MNRAS* **395**, 1409 (2009), arXiv:0809.0403 [astro-ph].
- [50] B. P. Schmidt, R. P. Kirshner, R. G. Eastman, M. M. Phillips, N. B. Suntzeff, M. Hamuy, J. Maza, and R. Aviles, *ApJ* **432**, 42 (1994).
- [51] R. G. Eastman, B. P. Schmidt, and R. Kirshner, *ApJ* **466**, 911 (1996).
- [52] L. Dessart and D. J. Hillier, *A&A* **439**, 671 (2005), arXiv:astro-ph/0505465 [astro-ph].
- [53] C. Vogl, S. Taubenberger, G. Csörnyei, B. Leibundgut, W. E. Kerzendorf, S. A. Sim, S. Blondin, A. Flörs, A. Holas, J. V. Shields, J. Spyromilio, S. H. Suyu, and W. Hillebrandt, arXiv e-prints , arXiv:2411.04968 (2024), arXiv:2411.04968 [astro-ph.CO].